ACS APPLIED MATERIALS & INTERFACES

Research Article

www.acsami.org

Selective Tumor Cell Inhibition Effect of Ni−Ti Layered Double Hydroxides Thin Films Driven by the Reversed pH Gradients of Tumor Cells

Donghui Wang,[†,§] Naijian Ge,[‡,§] Jinhua Li,[†] Yuqin Qiao,[†] Hongqin Zhu,[†] and Xuanyong Liu*[,†]

[†]State Key Laboratory of High Performance Ceramics and Superfine Microstructure, Shanghai Institute of Ceramics, Chinese Academy of Sciences, Shanghai 200050, China

[‡]Intervention Center, Eastern Hepatobilialy Surgery Hospital, the Second Military Medical University, Shanghai 200438, China

Supporting Information

ABSTRACT: Nitinol is widely fabricated as stents for the palliation treatment of many kinds of cancers. It is of great importance to develop nitinol stents with selective tumor cell inhibition effects. In this work, a series of pH sensitive films composed of $Ni(OH)_2$ and Ni−Ti layered double hydroxide (Ni−Ti LDH) with different Ni/Ti ratios were prepared on the surface of nitinol via hydrothermal treatment. The films with specific Ni/Ti ratios would release a large amount of nickel ions under acidic environments but were relatively stable in neutral or weak alkaline medium. Cell viability tests showed that the films can effectively inhibit the growth of cancer cells but have little adverse effects to normal cells. Besides, extraordinarily high intracellular nickel content and reactive oxygen species (ROS) level were found in cancer cells, indicating the death of cancer cells may be induced by the excessive intake of nickel ions. Such selective cancer cell inhibition effect of the films is supposed to relate with the reversed pH gradients of tumor cells.

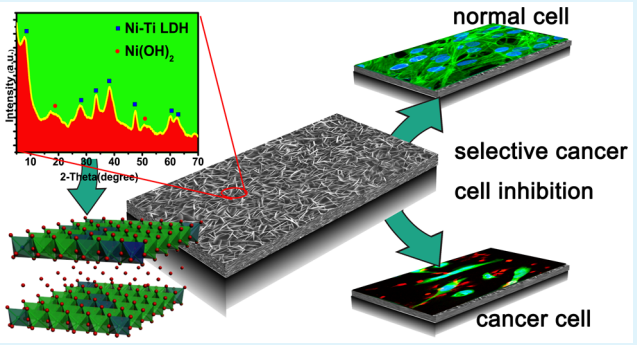

KEYWORDS: *nitinol, nickel, Ni−Ti layered double hydroxide, cancer, tumor, stent*

INTRODUCTION

Nitinol is a family of nearly equiatomic NiTi alloys with good biocompatibility and unique shape memory effects.[1,2] It has been widely fabricated as stents to help in the palliation of the malignant obstruction of bile duct, esophagus, trachea, and brochi[3−5] caused by many kinds of cancers.[6−9] However, currently used nitinol stents do not possess any tumor inhibition effects, and are susceptible to reocclusion induced by the tumor ingrowth and overgrowth.[10]

Nowadays, an important strategy to prevent cancer cell overgrowth is to incorporate antitumor drugs into a polymer coating on the surface of nitinol stents.[11−14] But the polymer used in the stents usually associated with serious cholecystitis and inflammatory responses. Besides, the released drugs may transport systemically and have adverse effects to the nontarget organs. Therefore, developing polymer free coatings with selective tumor inhibition properties is of great importance.

The key point to design materials with selective tumor inhibition effects is to find the differences between cancer cells and normal cells.[15] Previous studies have shown that tumor cells and normal cells differ markedly in energy metabolism. Normal cells produce energy mainly by mitochondrial oxidation. In contrast, tumor cells rely mostly on conversion of glucose into lactate for energy production.[16,17] To prevent acidosis, large amounts of lactates and hydrogen ions are pumped out of the cancer cells, leading to an acidic extracellular microenvironment but an alkalinized intracellular microenvironment,[18] which is contrary to normal cells. The reversed pH gradient of cancer cells has been recognized as a potential feature that can be utilized in targeting tumor cells. This is a very active research field, and many cancer cell targeting systems are designed based on this special property of cancer cells.[19] In most cases, the vital part of these platforms is a pH sensitive element that becomes reactive only in the existence of cancer cells.[20] Layered double hydroxides (LDHs) just have the sensitivity to pH,[21] and may be used in the selective tumor inhibition platform.

LDHs are a class of ionic lamellar compounds that have been widely used in the areas of catalysis,[22−24] separation[25,26] and precursors for function materials.[27−29] In particular, profiting from the biocompatibility, anionic-exchange and pH sensitive properties, layered double hydroxides are especially attractive being employed as biomaterials.[30,31] Jun-Kai Lin et al. directly grown Mg−Fe LDH on pure Mg and found that the LDH coated sample had a much higher corrosion resistance and a better cell spreading than the pure Mg alloy;[32] Feng Yao et al.

Received: September 7, 2014
Accepted: March 31, 2015
Published: March 31, 2015

DOI: 10.1021/acsami.5b01087
ACS Appl. Mater. Interfaces 2015, 7, 7843−7854

prepared a Mg−Al LDH array on gold substrate, which can promote selective cell adhesion;[33] Dae-Hwan Park et al. encapsulated DNA molecules into LDH and made it serve as an advanced gene delivery system;[34] Mingfei Shao et al. synthesized a three-component microsphere containing an SiO_2-coated Fe_3O_4 magnetite core and a Ni−Al LDH nanoplatelet shell, which can be used for the practical purification of recombinant proteins, as well as having other potential applications in a variety of biomedical fields including drug delivery and biosensors.[35] However, the potential inhibition effect of LDH to cancer cells has not been studied so far.

In this work, films composed of $Ni(OH)_2$ and Ni−Ti LDH with different Ni/Ti ratios were prepared on the surface of nitinol via simple hydrothermal treatment in sodium hydroxide solution. The Ni−Ti LDH films are very sensitive to acidic environments; therefore, more nickel ions will release in the existence of cancer cells owing to the low extracellular pH value. The released nickel ions transport into cells mainly through divalent metal transporter 1(DMT1), a proton pump coupling transport protein.[36,37] The large hydrogen chemical potential across cancer cell membrane induced by its reversed pH gradients can promote the uptake of nickel. In this way, the cytotoxicity nickel ions in Ni−Ti LDH will selectively "flow" to cancer cells and a selective tumor cell inhibition effect described above may be realized.

EXPERIMENTAL SECTION

Material Preparation and Characterization. A commercially available NiTi (50.8 at. % Ni) stick was cut into small cylinders with a diameter of 12 mm and thickness of 1 mm. The samples were ultrasonic cleaned in ethanol, deionized water and ultrapure water successively, and dried in ambient atmosphere for further use. The films on nitinol surface were prepared by hydrothermal treatment. Briefly, the nitinol plates were placed in a reaction vessel with Teflon liner, and a certain amount of NaOH (96%, Sinopharm Chemical Reagent, Shanghai, China) solution (5 mL for each plate) was gently poured into the vessel. The reaction vessels were then sealed and placed in an oven for 8 h with the temperature set to 120 °C. After the reaction, vessels were cooled in room temperature. Samples were gently rinsed with deionized water, dried in ambient atmosphere, boiled in ultrapure water for 1 h to decrease the surface nickel content. Then the samples were immersed in 0.1 M HCl solution for 2 h to dissolve the sodium hydroxide left on the surface. Finally, the films composed of Ni−Ti LDH and $Ni(OH)_2$ can be obtained. The concentration of the alkali used in the reaction was 2.5, 5 and 10 M, respectively, and the samples were designed as HT1#, HT2# and HT3# with the increasing concentration of NaOH.

The surface and cross section morphologies of the samples were characterized by field emission scanning electron microscopy (FE-SEM; S-4800, HITACHI, Japan). Powders scraped from the films were used to identify the crystalline phases of the samples by X-ray diffraction (XRD; D/Max, Rigaku, Tokyo, Japan). The elemental compositions of the sample surfaces were detected by energy dispersive spectrometry [EDS; equipped on the electron probe X-ray microanalysis system (EPMA, JAX-8100, Japan)] and X-ray photoelectron spectroscopy (XPS; RBD upgraded PHI-5000C ESCA system, USA) with an Mg Kα (1486.6 eV) source.

Metal Ions Release Measurement. All of the hydrothermal treated samples (HT1#, HT2# and HT3#) and the control sample NiTi were immersed in 10 mL of PBS (phosphate buffered saline) with different pH values at 37 °C without stirring for various periods of time. The amounts of released nickel and titanium were determined by analyzing the resulting solutions using inductively coupled plasma optical emission spectrometry (ICP-OES, Varian Liberty 150, USA). The pH value of the PBS was adjusted to 4.0, 6.8 and 7.4, respectively, with hydrochloride acid.

The nickel release amounts of samples with cells cultured on were also tested. 5×10^4 cells were seeded on each specimen. After the cells were cultured for different periods of time, the culture medium was collected and the nickel concentration was tested by ICP-OES.

Electrochemical Analysis. Dynamic potential polarization curves and cyclic voltammetry (CV) curves were acquired by a CHI760C electrochemical workstation (Shanghai, China). The electrochemical cell was assembled with a conventional three-electrode system: a saturated calomel electrode (SCE) as the reference electrode, a graphite rod as the counter electrode and the nitinol and all of the hydrothermal treated samples as the working electrodes. The polarization test was conducted in a physiological saline solution (0.9% NaCl at a pH of 7) and the voltammetric measurement was performed in a 0.5 M sodium hydroxide solution. Both of the tests were conducted at room temperature at a scanning rate of 10 mV/min.

Cell Viability Assay. The hepatoma carcinoma cell lines SMMC-7721 and HepG2 were obtained from Shanghai Oriental Gallbladder Hospital; cholangiocarcinoma cell line RBE was purchased from Cell Bank of Chinese Academy of Science; human intrahepatic biliary epithelial cells (HIBEpic) were from Sciencell. All of the cell lines were maintained in the media provided by suppliers, in a humidified atmosphere of 5% CO_2 at 37 °C. Based on the cell condition, cells were passaged at a ratio of 1:2−1:3 every 2−4 days.

The cell proliferation was determined by using the alamarBlue assay (AbD Serotec Ltd., UK). Cells were seeded on the specimens with a density of 5×10^4 cells/well. Four specimens were tested for each incubation period (1, 4 and 7 days). After each incubation period, the culture medium was removed and 1.0 mL of the fresh medium with 10% alamarBlue was added to each well. After incubation for 4 h, 100 μL of the culture medium was transferred to a 96-well plate for measurement. Accumulation of reduced alamarBlue in the culture medium was determined by an enzyme labeling instrument (BIO-TEK, ELX 800) at excitation wavelengths of 570 and 600 nm. The cell proliferation rate was calculated according to the instruction of the alamarBlue assay.

Live/Dead Cell Staining. The live−dead cell staining kit (Biovision, USA) was used according to manufacturer's instructions. Briefly, cells were seeded on the specimens with a density of 5×10^4 cells/well, and cultured for 24h. Then propidium iodide (PI) and calcium-AM were diluted to a final concentrations of 5 and 2 μM in PBS, respectively. 100 μL of mixed solution was added to each specimen, and the cells were stained at 37 °C for 15 min.

Intracellular Nickel Concentration. 1×10^5 cells were planted on each sample, and cultured for 24 h. Then medium was removed, and the surfaces were washed with PBS twice and the cells were collected by trypsinization and counted using a hemocytometer. Cells were then centrifuged and resuspended in 500 μL of nitrid acid. The cell lysis was maintained at 80 °C for 4 h and then diluted with 4 mL of water. Nickel concentration was measured by ICP-OES and normalized against cell number.

Oxidative Stress Level Measurement. Cells were seeded on the specimens with a density of 1×10^5cell/well, and cultured for 24 h. Next, cells were washed three times with PBS. A mixture of 2′,7′-dichlorodihydrofluorescein diacetate (DCFH-DA, final concentration of 10 μM Sigma-Aldrich, USA) solution was added to the cells for 30 min at 37 °C. The reactive oxygen species (ROS) level was obtained from the fluorescence reading of 2′,7′-dichlorescein (DCF; Ex 488 nm/Em 535 nm) by confocal laser scanning microscopy (CLSM, Leica SP8, Germany), and normalized against the cell numbers. Results were expressed as fold increase of ROS with respect to that of cells incubated on nitinol.

Cytoskeleton Stain. Samples were placed in a 24-well plate, and the cells were seeded on the surface of the samples at a density of 1×10^5 cells/well. After incubatiion for 1, 4 and 24 h, the seeded cells were rinsed with PBS three times. Then cells were fixed, permeabilized and blocked successively by 4% paraformaldehyde (PFA) diluent, 0.1% (v/v) Triton X-100 (Amresco, USA) and 1 wt % bovine serum protein (BSA, Sigma, USA) respectively. After each step, cells were rinsed with PBS. Then fluorescein isothiocyanate (FITC) phalloidin was added to

DOI: 10.1021/acsami.5b01087
ACS Appl. Mater. Interfaces 2015, 7, 7843−7854

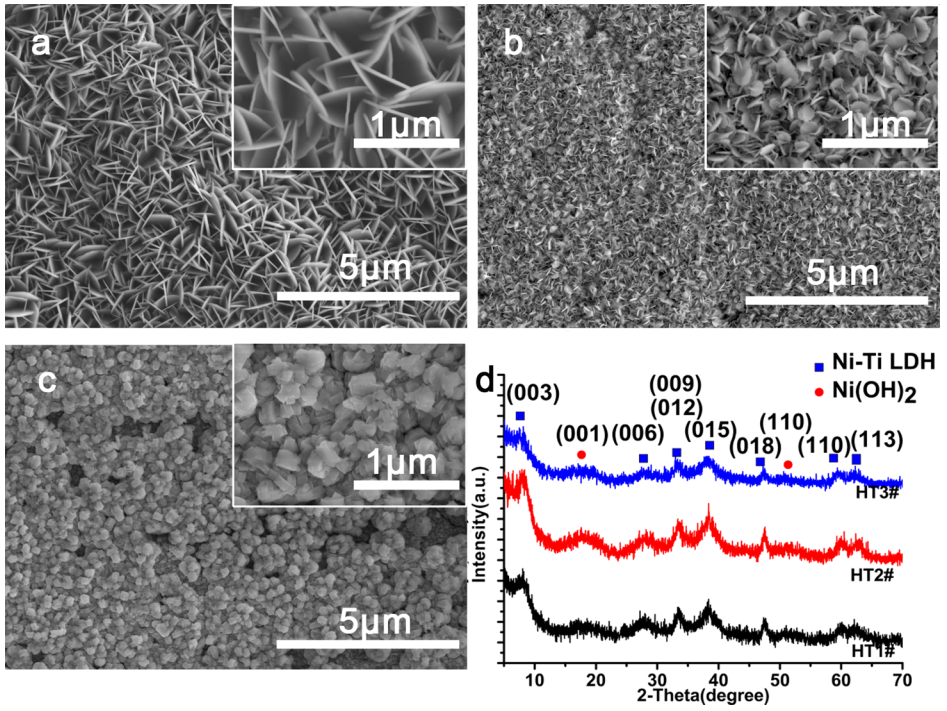

Figure 1. SEM morphology of HT1 (a), HT2 (b) and HT3 (c) at low and high magnification; XRD patterns acquired from the hydrothermal treated samples (d).

stain F-actin, followed by rinsing with PBS and further staining nucleus with DAPI (Chemical International).

Cell Imaging. SEM and CLSM were used to acquire images of cells. Cells for SEM observation were fixed in 2.5% glutaraldehyde for 4 h at 4 °C. Then the specimens were dehydrated in a series of ethanol solutions (30, 50, 75, 90, 95 and 100 v/v%) for 10 min, followed by drying in the hexamethyldisilizane (HMDS) ethanol solution series (33, 50, 66 and 100 v/v%) for 10 min each series sequentially.

Specimens for CLSM observation were protected from light and preserved at 4 °C. Cells were fixed in 4% PFA and were observed in 1 week after staining.

Statistical Analysis. All statistical analysis was carried out using a GraphPad Prism 5 statistical software package. All the data were expressed as means ± standard deviation (SD). Statistically significant differences (P) between the various groups were measured using one-way analysis of variance and Tukey's multiple comparison tests. A value of $p < 0.05$ was considered to be statically significant, and was represented by the symbol "*", a value of $p < 0.01$ was represented by "**", and $p < 0.001$ was "***".

RESULTS AND DISCUSSION

Formation of Ni−Ti LDH. Figure 1a,b,c depicts the surface morphologies of nitinol discs treated by the hydrothermal reactions. A nanoflake-like structure appears after hydrothermal treatment in 2.5 M sodium hydroxide. With increasing sodium hydroxide concentration, the surfaces still maintain a nanoflake-like topography, but the nanoflakes curl up and become more densely distributed. These nanoflakes transform to "wool ball"-like structures completely as the concentration of sodium hydroxide reach 10 M. The diameter of the "ball" was about 500 nm, while the width of the "wool" was about 100 nm.

The XRD pattern of the samples is shown in Figure 1d. The X-ray diffraction of the hydrothermal treated samples show basal peaks corresponding to (0 0 3), (0 0 6) and (0 0 9) and nonbasal peaks corresponding to (0 1 2), (0 1 5), (0 1 8), (1 1 0) and (1 1 3) reflections of Ni−Ti LDH.[38−40] The left peak centered at 19° can be assigned to nickel hydroxide,[41] as this peak is broad and weak, it can be deduced that the nickel hydroxide contents in these films are very low, and mainly existed in amorphous phase.

The specimens were further investigated by XPS. The surface compositions of the samples detected by XPS are shown in Table 1, three elements titanium, nickel and oxygen are detected on the surfaces of the samples. The titanium contents decrease with the concentration rise of sodium hydroxide while the nickel contents increase, leading to an increasing Ni/Ti ratio. However, only a small variation of oxygen content can be found among different samples. Figure 2 shows the XPS Ni 2p, Ti 2p and O 1s spectra obtained from the surface of all of the hydrothermal treated samples. Four 2p peaks of nickel centered at 856.0 eV (Ni $2p^{3/2}$), 861.7 eV(Ni $2p_{3/2}$, sat), 873.7 eV (Ni $2p_{1/2}$) and 880.0 eV (Ni $2p_{1/2}$, sat) are assigned to the typical nickel peaks of Ni−OH.[42] The XPS spectra of Ti 2p indicate two peaks centered at 464.2 eV (Ti $2p_{1/2}$) and 458.4 eV (Ti $2p_{3/2}$), corresponding to the binding energies of Ti^{4+} in $Ti(OH)_6^{2-}$.[43] The O 1s peak can be divided into two peaks centered at 530.3 and 531.5 eV corresponding to oxygen peak in hydroxyl bonding with Ti and Ni, respectively.[42,44,45] The XPS results further confirm the existence of Ni−Ti LDH on the surfaces of all of the treated samples.

Table 1. Elemental Compositions of NiTi Surface before and after Hydrothermal Treatment

	Ti (at. %)	Ni (at. %)	O (at. %)	Ni/Ti
NiTi	17.1 ± 1.83	4.0 ± 0.72	78.9 ± 2.35	0.2 ± 0.03
HT1#	12.9 ± 0.49	20.7 ± 1.74	66.6 ± 2.23	1.6 ± 0.08
HT2#	5.3 ± 0.56	26.4 ± 2.94	68.3 ± 3.46	5.0 ± 0.21
HT3#	4.0 ± 0.72	28.2 ± 4.59	67.8 ± 5.29	7.1 ± 0.34

Scheme 1i,ii depicts the process of the formation of Ni−Ti LDH, which can be explained by the in situ growth of nickel

DOI: 10.1021/acsami.5b01087
ACS Appl. Mater. Interfaces 2015, 7, 7843−7854

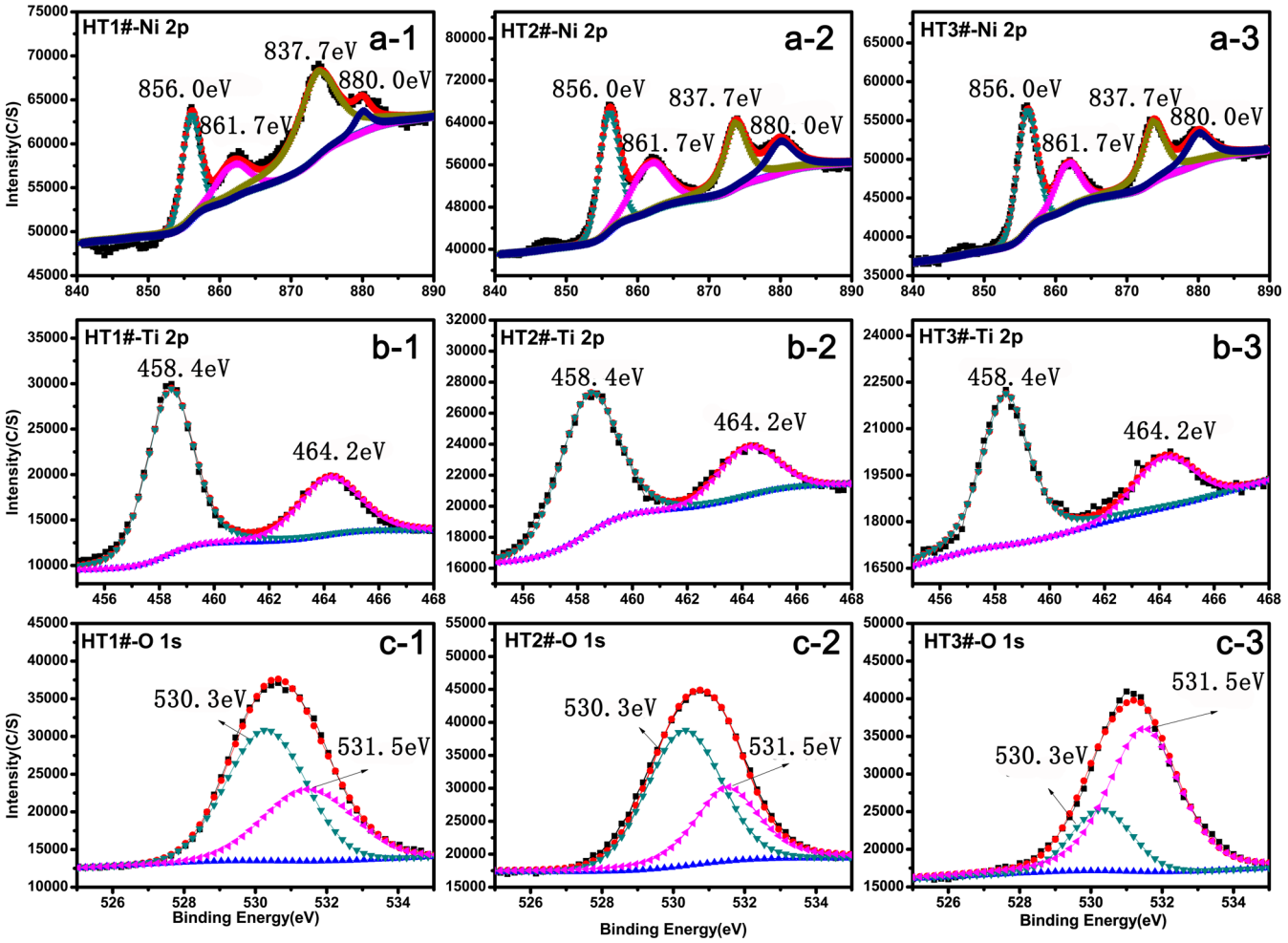

Figure 2. XPS of Ni 2p (a–i), Ti 2p (b–i) and O 1s (c–i) [i: 1, 2 and 3 represent HT1#, HT2# and HT3#, respectively].

Scheme 1. Schematic Diagram Depicting the Formation of Ni–Ti LDH[a]

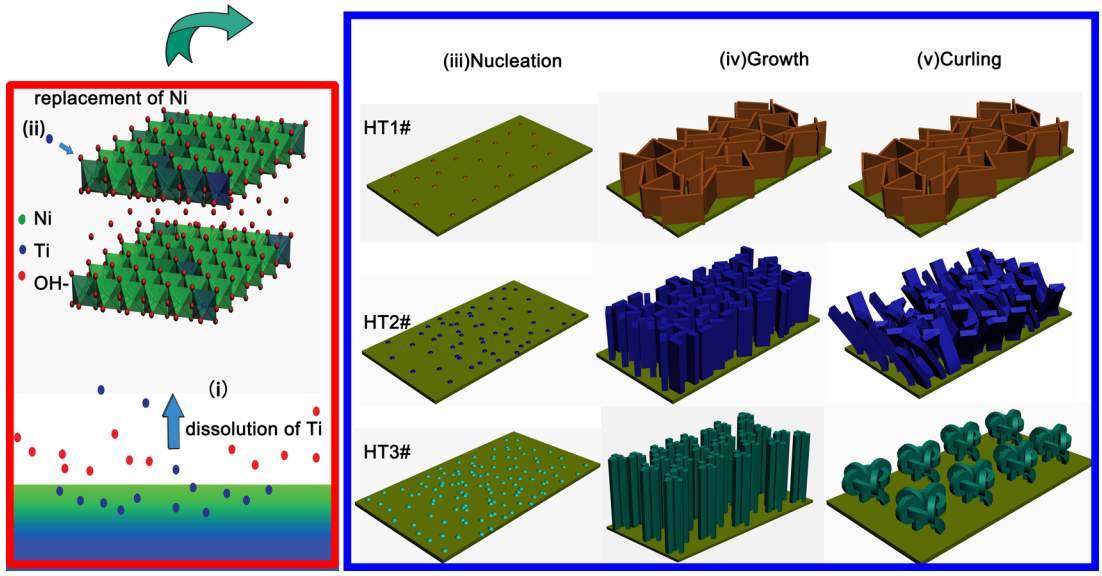

[a](i) The dissolution of titanium; (ii) local nucleation of nickel hydroxide followed by the replacement of nickel by titanium; (iii) nucleation of Ni–Ti LDH; (iv) growth of Ni–Ti LDH crystal; (v) curling of the crystal in the force of surface tension.

hydroxide, followed by its transformation to the layered double hydroxide with the dissolved titanium in the hot liquid. Titanium and nickel are different in reactivity, so there will be a selective oxidation in the first stage of the hydrothermal

DOI: 10.1021/acsami.5b01087
ACS Appl. Mater. Interfaces 2015, 7, 7843–7854

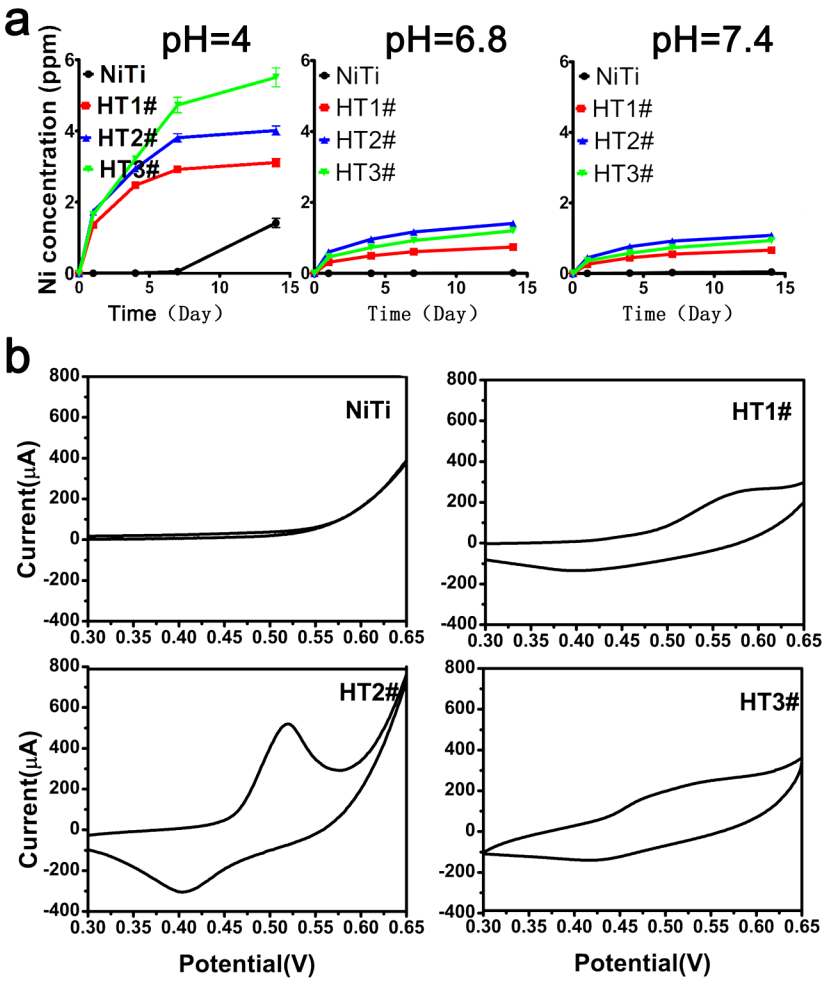

Figure 3. Cumulative nickel release amounts in PBS with different pH (a), and the cyclic voltammetry curve of NiTi and the treated samples (b).

treatment,[46,47] titanium will be preferentially oxidized to $Ti(OH)_6^{2-}$ and dissolved in the sodium hydroxide solution.[48] After titanium dissolves, the bonds between titanium and nickel are broken, leading to the energy increase of nickel atom.[46] To lower the energy, nickel atoms also tend to react with OH^-, resulting in the nucleation of nickel hydroxide. Then some dissolved titanium ions in the solution will transport to the lattice of $Ni(OH)_2$ and replace nickel ions. The extra charges induced by the replacement will be balanced by the anions (OH^-) between layers, and Ni−Ti LDH can be got. However, there are still some $Ni(OH)_2$ crystals can be detected from the sample surfaces, besides the nickel content on the sample surface is much bigger than that of titanium. Therefore, it can be deduced that only a small portion of the dissolved titanium can enter into the nickel hydroxide lattice, most of the dissolved titanium is left in the solution. With the increasing concentration of sodium hydroxide, more titanium will be dissolved, so more titanium will be left in the solvent, leading to the increase Ni/Ti ratio on the sample surfaces.

Two types of nanostructures (the nanoflake like structure in two types of dimension and the wool sphere nanoarchitectures) were obtained on nitinol surfaces. As shown in Scheme 1iii,iv,v, the formation of the different nanostructures basically involves three processes: nucleation, growth and curling. The details of each process are discussed in the Supporting Information.

Physico-Chemical Property of Ni−Ti LDH. Nickel, as an essential element in the human body, is known to be allergenic and toxic.[36,49] The nickel release amount is one of the major factors affecting cellular behaviors.[50] Figure 3a presents the cumulative release amounts of nickel ions as a function of immersion time in PBS with different pH. It can be found that samples' nickel release amounts increase with the decrease of pH value. HT3# exhibits the highest pH sensitivity. It has the largest nickel release amounts among all of the samples at pH = 4, but relatively stable in neutral and weak alkaline environments, in which conditions, its nickel release amounts are smaller than that of HT2#. Such pH sensitivity of HT3# may be resulted from its specific Ni/Ti ratio. As shown in Scheme 2, it is supposed that nickel ions can be released outside via two pathways. In the neutral and weak alkaline environments, nickel ions mainly transport outside through the defects exit in the material. As mentioned above, ion replacement takes place in the formation of LDH, the replacement will induce lattice imperfection, which will facilitate ions diffusion and release. With the highest Ni/Ti ratio, there are few nickel ions being replaced by titanium in HT3#, leading to its low defects concentration. Therefore, few nickel ions can leach out from HT3# in the neutral and weak alkaline environment. While, in acidic environment the nickel release is mainly induced by the reaction between hydrogen ions and the alkaline Ni−Ti LDH. The replacement of Ni^{2+} by Ti^{4+} will generate positive charges on the frameworks of LDH. The electrostatic repulsion between H^+ and the positive charges will inhibit the reaction between hydrogen ions and LDH. Therefore, samples with

DOI: 10.1021/acsami.5b01087
ACS Appl. Mater. Interfaces 2015, 7, 7843−7854

Scheme 2. Illustration of the Mechanism of Nickel Ions Release[a]

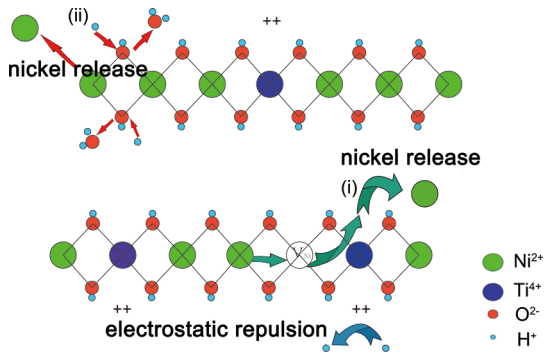

[a](i) Nickel ions move out through the defects in the film; (ii) nickel ions release induced by the reaction between the prepared film and the hydrogen ions in the environment.

more positive charges on the surface will release less nickel ions. With the highest Ni/Ti ratio, few positive charges exit on sample HT3. Hydrogen ions can easily approach and attack it, leading to the highest nickel release amounts of HT3# in acidic environment. It should be noted that, HT1# always has the lowest nickel release no matter what the pH is. This phenomenon may be induced by the lowest nickel content on HT1# surface.

The nickel release amount is likely related to the corrosion resistance and reactivity of samples. So, the dynamic potential polarization tests and cyclic voltammetry tests were conducted. The Tafel plots and resulting data are exhibited in Figure S5 of the Supporting Information and Table 2. It can be seen that

Table 2. Parameters Obtained by the Tafel Polarization Method

	NiTi	HT1#	HT2#	HT3#
Icor (A)	1.4×10^{-6}	7.4×10^{-7}	2.2×10^{-6}	5.6×10^{-7}
Ecor(V) vs SCE	−0.25	−0.34	−0.30	−0.21

HT3# has the highest corrosion potential followed by HT2# and HT1#, indicating that samples with higher Ni/Ti ratio is harder to be corroded in thermodynamics. This result can be ascribed to the decreasing crystal defects with the increasing Ni/Ti ratio of the samples. The corrosion currents are related to the samples' corrosion resistance in kinetics, which is affected by ions release rate of the samples. It can be found that HT2# has the highest corrosion current whereas HT3# has the lowest, basically in according with the nickel release profile of different samples in neutral environments.

Figure 3b shows the CV curves of all of the samples. Obvious cathodic and anodic peaks, assigned to the Ni^{2+}/Ni^{3+} redox,[51,52] can be seen in the CV curve of sample HT2#. Peaks in the same potions also existed in the CV curves of HT1# and HT3#, but the peak height is much lower. The appearance of cathodic peaks can be ascribed to the proton transfer, which resulted in the transform of Ni^{2+} to Ni^{3+}. Crystal defects existed in the films will facilitate the proton transfer. Sample HT3# has the fewest crystal defects, so the cathodic peak of HT3# is the lowest among all of the samples. The relative low cathodic peak of HT1# may result from the large amounts of positive charges existing on it. These positive charges will inhibit the proton transfer through electrostatic repulsion.

Cell Viability. The viability of cancer cells (RBE) and normal cells (HIBEpic) cultured on different samples was determined by the alamarBlue assay, and the results are shown in Figure 4. With regard to cancer cells, nearly no differences can be observed after 1 day of culturing. However, after culturing for 4 and 7 days, the cells on HT1# show an obvious higher proliferation rate than that on NiTi. On the contrary, cells on HT2# and HT3# present much lower viabilities. Especially, the number of cells on HT3# even decreased along with time, indicating that sample HT3# is cytotoxic to cancer cells. However, sample HT3# shows less adverse effects to normal cells, and it even promote cell proliferating in the first 4 days of culturing. The morphologies of cells having been cultured on the sample surfaces for 4 days are depicted in Figure 5a,b. For cancer cells, NiTi and HT1# are nearly completely covered by cells, but only a few cells can be found on the surfaces of HT2# and HT3#. Besides, a lot of cells on HT3# still keep a round or spindle morphology, whereas on other samples, cells present a multipolar spindle morphology. With regard to normal cells, all of samples were covered by cells completely without differences. Figure 5c,d shows the results of live/dead staining. There are nearly no dead normal cells that can be detected from all of the sample surfaces, but many dead cancer cells can be found on the surface of HT3#. The results above indicate that the sample HT3# can effectively inhibit the growth of tumor cells but has little adverse effects on normal cells. Two other cancer cell lines, SMMC-7721 and HepG2, were also cultured on the samples, and the cell viabilities were tested. The result is presented in Figure S6 of the Supporting Information show that the growth of these two cancer cell lines could also be inhibited by HT3#. As the surface nickel content of sample HT3# is very high, the selective tumor cell inhibition effect may result from the cytotoxic element nickel.

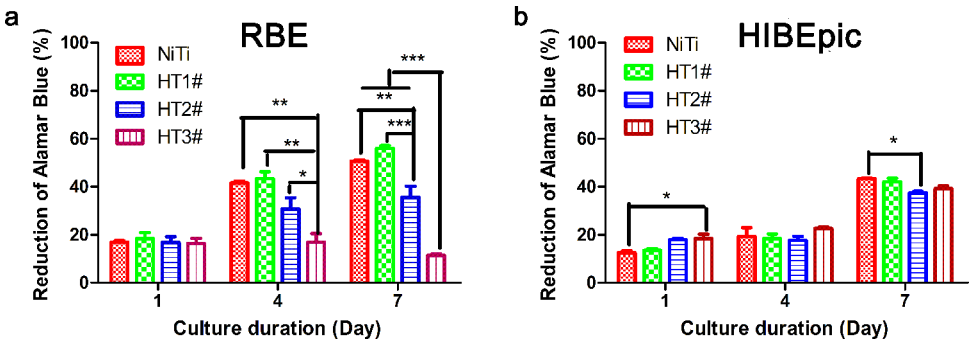

Figure 4. Reduction percentage of alamarBlue for RBE cells (a), and HIBEpic cells (b) cultured for various periods of time on the various surfaces.

DOI: 10.1021/acsami.5b01087
ACS Appl. Mater. Interfaces 2015, 7, 7843−7854

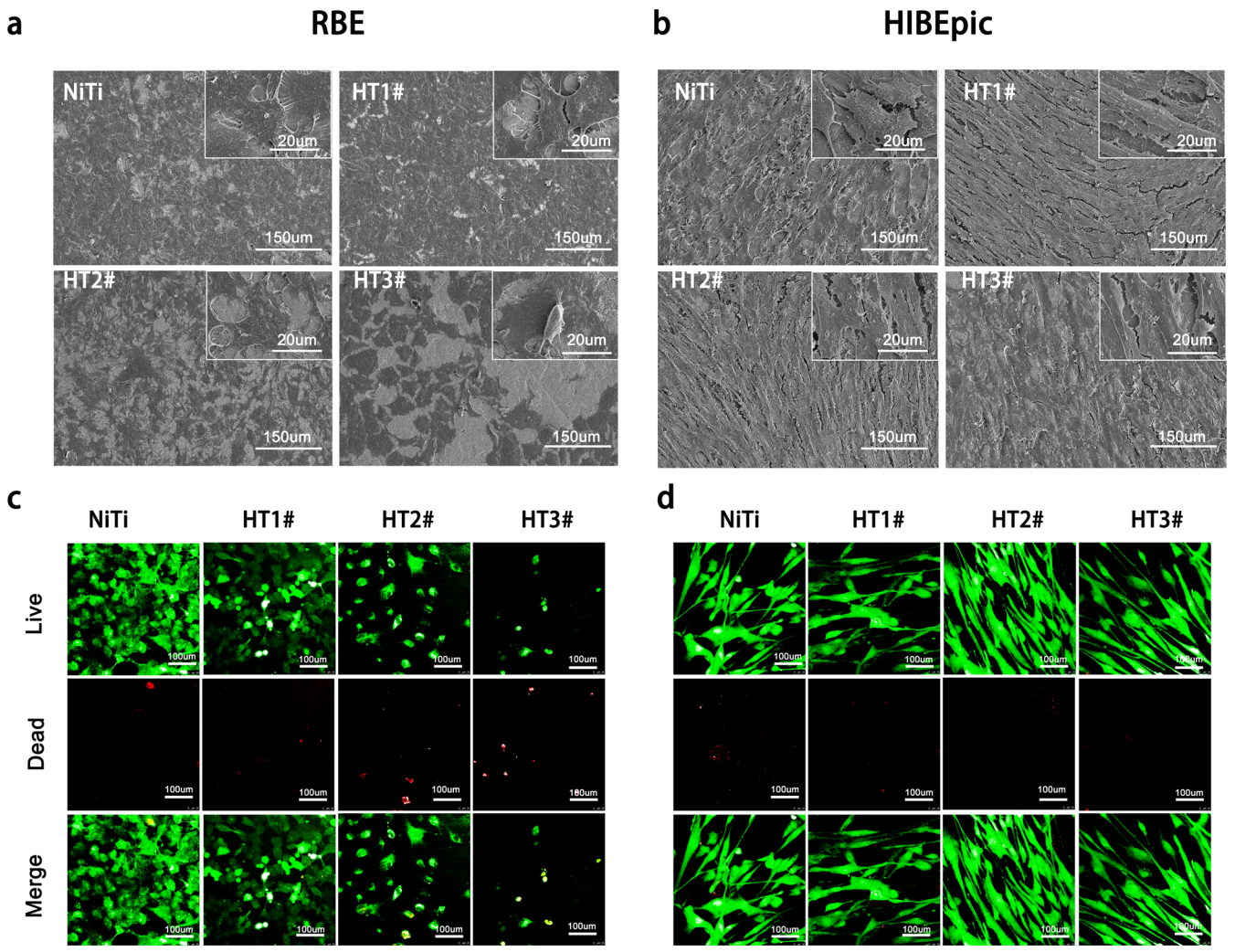

Figure 5. SEM morphology of RBE cells (a) and HIBEpic cells (b) after 4 days of culturing on various surfaces; the CLSM images of live/dead staining of RBE cells (c) and HIBEpic cells (d) after 4 days of culturing on various surfaces.

Many studies have shown that nickel is toxic at high concentrations.[36,49,53] Nickel ion is an oxidant that promotes oxidative chemistry in the cytosol and nucleus through participation in Fenton chemistry, a process that generates the production of reaction oxygen species (ROS).[36] These ROS compounds are very reactive and can go on to participate in reactions with biomolecules, leading to membrane damage and lipid peroxidation. Moreover, generation of oxidative stress and ROS has been shown to play a major role in cell apoptosis through a caspase-3 dependent pathway.[54] Therefore, the intracellular nickel concentrations and ROS levels of cancer cells and normal cells were tested. Results are presented in Figure 6. An extraordinarily high intracellular nickel concentration and ROS level is found in cancer cells cultured on sample HT3#, while the nickel concentration and ROS content in normal cells cultured on different samples show no significant differences and stay in a relatively low level. These results indicate that the selective tumor cell inhibition effect of HT3# is correlating with the selective "flow" of nickel from samples to cancer cells.

To investigate why nickel ions will selectively flow to cancer cells, the samples' nickel release profile with cancer cells and normal cells cultured on were tested. The results are presented in Figure 7, and it can be found that more nickel ions will be released from samples with cancer cells cultured on than those with normal cells. Especially, HT3# is the most sensitive sample, it has the highest nickel release amounts in the existence of cancer cells, but only a few nickel ions can release from it with normal cells cultured on. Such big differences in nickel release amounts of HT3# may stem from the reversed pH gradients of cancer cells. As shown in Scheme 3, normal cells and cancer cells differ markedly in energy metabolism. The process of glucose metabolize in normal cells, involves cytoplasmic glycolysis as well as mitochondrial citric acid cycle and electron transport chain, resulting in the completely oxidizing of glucose. In contrast, glycolysis is the major metabolism mode for cancer cells.[15,55] The abnormally high glycolytic metabolism produces a lot lactate acid in cancer cells. To prevent acidosis, Na^+/H^+ exchanger isoform 1 (NHE1) is overexpressed on cancer cells' membranes. This protein can pump out hydrogen ions, leading to an alkaline intracellular environment and an acidic extracellular environment, which is the reverse to normal cells.[18,56,57] In this study, we found that after culturing cancer cells for 3 days, the pH of the medium decreased from 7.45 to 6.90, but with regard to normal cells, nearly no decrease of medium pH could be detected (from 7.40 to 7.38). As the prepared films are very sensitive to pH, with

DOI: 10.1021/acsami.5b01087
ACS Appl. Mater. Interfaces 2015, 7, 7843−7854

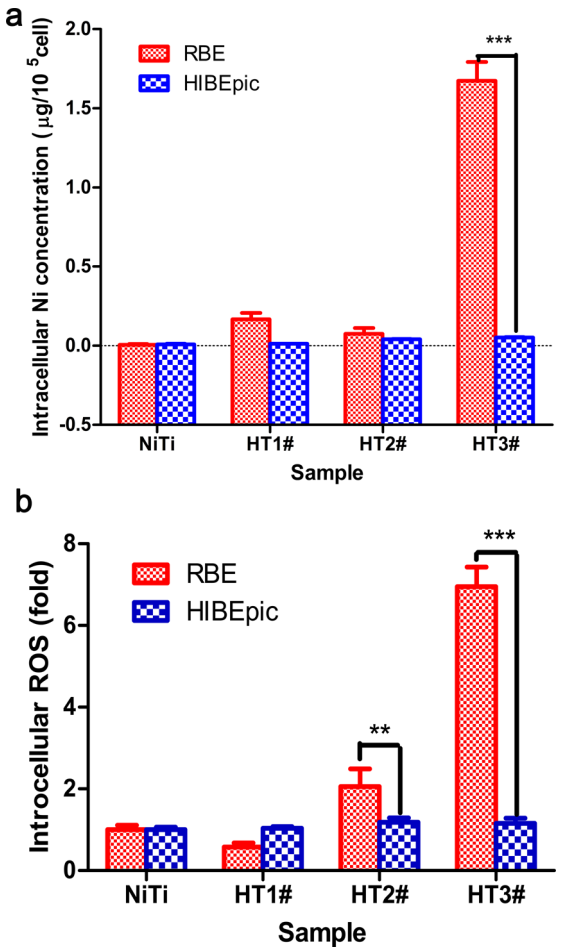

Figure 6. Introcellular nickel concentration (a) and ROS level (b) of RBE and HIBEpic after culturing on various surfaces for 24 h.

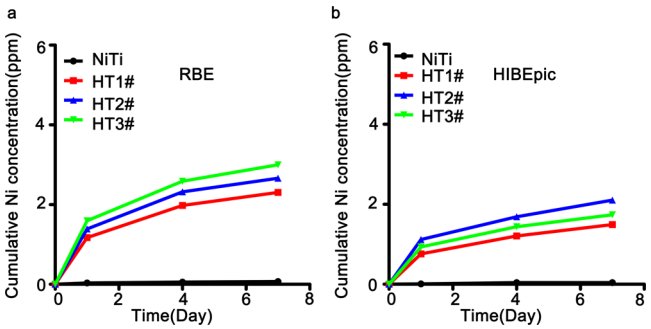

Figure 7. Cumulative nickel release amounts of NiTi and the treated samples with cancer cells (a) and normal cells (b) cultured on the sample surfaces.

different types of cells cultured on, the samples' nickel release amounts will change accordingly.

The released nickel ions enter into cells mainly through a cell membrane transporter. It has been reported that divalent metal transporter 1 (DMT1), a proton pump coupling transport protein,[36,37] has an important role in the uptake of nickel. This nickel transporter is energized by the H^+ electrochemical potential gradient.[58−61] Due to the reversed pH gradients, the hydrogen electrochemical potential across cancer cells' membrane is much larger than that of normal cells. It is much easier for nickel ions to enter into cancer cells through DMT1. Therefore, cancer cells are supposed to be more sensitive to nickel, which has been verified by the IC50 curve of nickel for cancer cells and normal cells (Figure S7 in the Supporting Information). As shown in Scheme 3, a high nickel release amount and high nickel uptake result in the extraordinarily high intracellular nickel concentration of cancer cells cultured on sample HT3#. The intracellular nickel ions induce lots of ROS, and finally leading to the apoptosis of cancer cells. Acidic materials will leach out from the dead cells, which will further promote the nickel release and uptake.

With regard to normal cells, their weak alkaline microenvironment will inhibit the function of DMT1, and nickel ions absorption will mainly via free diffusion. The intracellular nickel concentration will be linearly correlated to the nickel concentration in the environment. As verified above, the nickel release amounts of HT3# with normal cells cultured on is relatively low, and few nickel ions can enter into the cells. Therefore, HT3# shows nearly no adverse effects to normal cells.

It is noteworthy that nanotopgraphy of samples is also an important factor that may affect cell behavior.[62−64] In vitro studies have identified nanoscale features as potent modulators of cellular behavior through the onset of focal adhesion formation.[65] To explore the initial cell adherence process, the cytoskeleton of cancer cells RBE and normal cells HIBEpic seeded on all of the samples were observed by CLSM. The results are presented in Figure 8. After 1 h of incubation, normal cells on HT2# and HT3# present a spindle morphology. Cells on NiTi and HT1# show round morphologies, and the spindle shaped cells can hardly be found until incubation for 4 h. After 24 h of incubation, cells on all of the samples show a fibrous structure but there are more cells adhered on the surfaces of HT2# and HT3#. These results indicated that samples HT2# and HT3# can effectively promote the adhesion and spreading of normal cells, whereas HT1# has adverse effects to cell adhesion. In the case of cancer cells, HT2# and HT3# also show promotion effects on cell spreading at the initial stage. Cells present a round and less spread morphology on NiTi and HT1# but a well spread mutipolar spindle morphology on the samples HT2# and HT3# in the first hour. However, after 4 h of incubation, the promotion effect disappears. Fewer cells can be detected on the sample HT2# and HT3# compare to NiTi and HT1#. The inhibition effect becomes more obvious after 24 h of incubation.

Work by Arnold et al. showed that focal adhesion assembly requires that spacing between ligated integrins be less than 70 nm.[66] Large spacing between nanoprotrusions will limit the formation of focal adhesion and inhibit the spread of cells.[67] In this study, spacing between nanostructures of HT1# is the largest among all of the samples, leading to its adverse effects to cell spreading. On the contrary, cells spread much better on samples HT2# and HT3#, which may be owing to the densely distributed nanostructures on these samples provide enough binding site for the formation of focal adhesion. Better spreading and adhesion usually means a higher cell proliferation rate.[65] It is true in the condition that cells were cultured on samples without nickel release (Figure S8b in the Supporting Information). But with nickel release, better spreading means bigger contact area between cells and the sample surfaces, so the possibility of nickel on the sample surface intake by cells increases, and more nickel will enter into cells.

Therefore, the selective tumor cell inhibition effect of HT3# is the combined effect of the sample chemical component,

DOI: 10.1021/acsami.5b01087
ACS Appl. Mater. Interfaces 2015, 7, 7843−7854

Scheme 3. Illustration for the Possible Mechanism of the Selective Tumor Inhibition Effect[a]

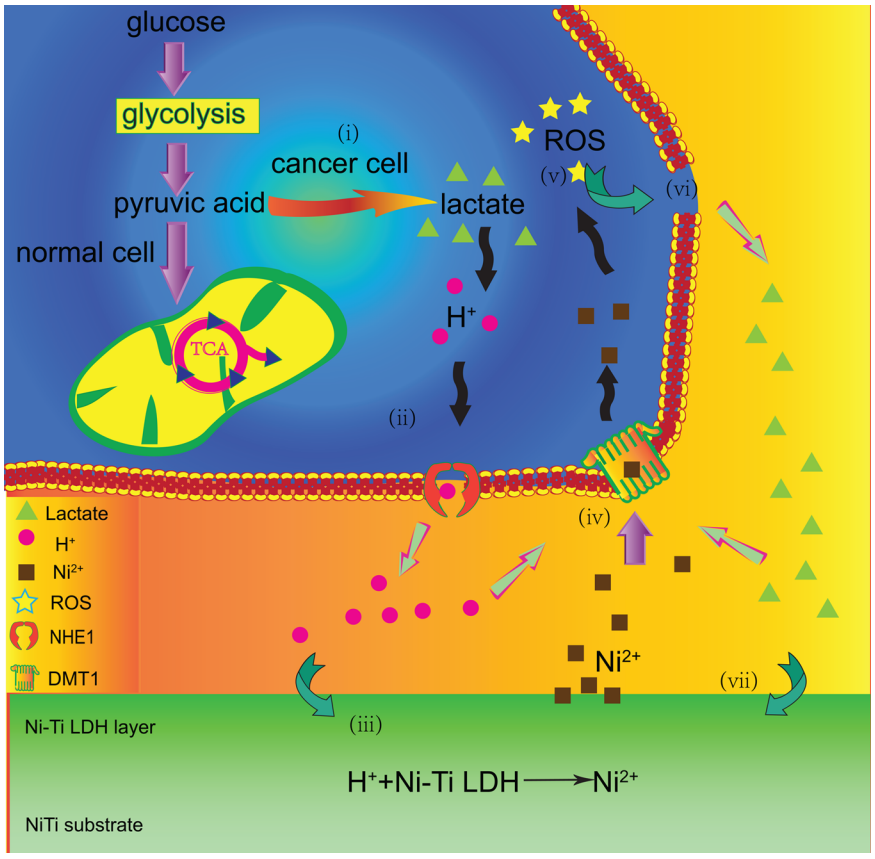

[a](i) Unique metabolic way of cancer cells resulting in a lot of lactate production; (ii) hydrogen ions are pumped out of cancer cells by NHE1, leading to a reversed pH gradients of cancer cells; (iii) nickel is dissolved from Ni−Ti LDH because of the low pH environment; (iv) the reversed pH gradient promotes the nickel uptake by cancer cells via DMT1; (v) nickel induces the production of ROS; (vi) apoptosis or necrosis resulting from the high level of intracellular ROS; (vii) acidic materials leach out from the dead cells, which further promotes the nickel release and uptake by cancer cells.

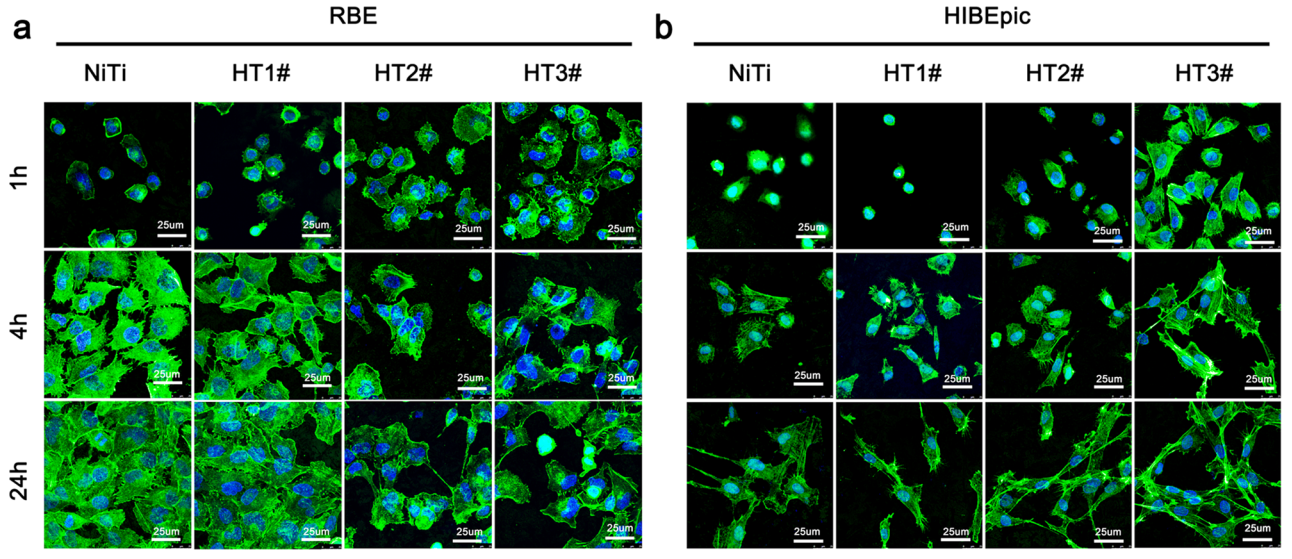

Figure 8. CLSM images of RBE cells (a) and HIBEpic cells (b) cultured for 1, 4 and 24 h on various surfaces with F-actin stained with FITC (green) and the nucleus stained with DAPI (blue).

topography and the unique features of cancer cells. The special chemical component that makes the nickel release amount can be adjusted by pH; the topography makes the surface promote cell spreading, increasing the nickel uptake possibility; the reversed pH gradients of cancer cells promote nickel release and uptake.

DOI: 10.1021/acsami.5b01087
ACS Appl. Mater. Interfaces 2015, 7, 7843−7854

CONCLUSION

Films composed of Ni−Ti LDH and $Ni(OH)_2$ were successfully prepared on the surface of nitinol, via a simple hydrothermal treatment. The specimens with the highest Ni/Ti ratio (7:1) can effectively inhibit the growth of many kinds of cancer cell lines investigated in this study (including RBE, SMMC-7721 and Hep-G2), but have little adverse effect to normal cells. The selective tumor cell inhibition effect is supposed to be driven by the reversed pH gradient of cancer cells, and the Ni/Ti ratio of films was an important factor affecting the selectivity of the samples. The prepared film in this study shows great potential in the palliation treatment of cancers. But the present work just shows the results of the in vitro cytotoxicity tests, and further in vivo studies are needed to confirm the safety of this film.

ASSOCIATED CONTENT

Supporting Information

XPS full spectra, SEM images of cross section, EDS patterns of samples before and after acid treatment, titanium release profile, polarization curves, IC50 curves of nickel for RBE and HIBEpic, effects of the samples to other cancer cell lines proliferation, effects of nickel release and nanotopography to cancer cell proliferation. This material is available free of charge via the Internet at http://pubs.acs.org.

AUTHOR INFORMATION

Corresponding Author

*Prof. Xuanyong Liu. E-mail: xyliu@mail.sic.ac.cn. Tel.: +86 21 52412409. Fax: +86 21 52412409.

Author Contributions

§These authors contributed equally to this work.

Notes

The authors declare no competing financial interest.

ACKNOWLEDGMENTS

Financial support from the National Basic Research Program of China (973 Program, 2012CB933600), National Natural Science Foundation of China (81271704, and 31200721), Shanghai Committee of Science and Technology, China (13441902400, 14XD1403900 and 14JC1493100) is acknowledged.

REFERENCES

(1) Wever, D. J.; Veldhuizen, A. G.; Sanders, M. M.; Schakenraad, J. M.; van Horn, J. R. Cytotoxic, Allergic and Genotoxic Activity of a Nickel-Titanium Alloy. *Biomaterials* **1997**, *18*, 1115−1120.

(2) Wever, D. J.; Veldhuizen, A. G.; de Vries, J.; Busscher, H. J.; Uges, D. R. A.; van Horn, J. R. Electrochemical and Surface Characterization of a Nickel-Titanium Alloy. *Biomaterials* **1998**, *19*, 761−769.

(3) Mauro, M. A.; Koehler, R. E.; Baron, T. H. Advances in Gastrointestinal Intervention: The Treatment of Gastroduodenal and Colorectal Obstructions with Metallic Stents. *Radiology* **2000**, *215*, 659−669.

(4) Duerig, T.; Pelton, A.; Stockel, D. An Overview of Nitinol Medical Applications. *Mater. Sci. Eng., A* **1999**, *273*, 149−160.

(5) Mani, G.; Feldman, M. D.; Patel, D.; Agrawal, C. M. Coronary Stents: A Materials Perspective. *Biomaterials* **2007**, *28*, 1689−1710.

(6) Cwikiel, W.; Stridbeck, H.; Tranberg, K. G.; Vonholstein, C. S.; Hambraeus, G.; Lillogil, R.; Willen, R. Malignant Esophageal Strictures - Treatment with a Self-Expanding Nitinol Stent. *Radiology* **1993**, *187*, 661−665.

(7) Smith, A. C.; Dowsett, J. F.; Russell, R. C. G.; Hatfield, A. R. W.; Cotton, P. B. Randomized Trial of Endoscopic Stenting versus Surgical Bypass in Malignant Low Bileduct Obstruction. *Lancet* **1994**, *344*, 1655−1660.

(8) Lee, B. H.; Choe, D. H.; Lee, J. H.; Kim, K. H.; Chin, S. Y. Metallic Stents in Malignant Biliary Obstruction: Prospective Long-Term Clinical Results. *Am. J. Roentgenol.* **1997**, *168*, 741−745.

(9) Mathur, S.; Mujtaba, G.; Sonpal, N.; Arya, M. Successful Closure of a Tracheo-esophageal Fistula Using a Metal Stent Endoscopically. *Am. J. Gastroenterol.* **2010**, *105*, S167−S167.

(10) Lee, D. K.; Jang, S. I. Drug-Eluting Stent in Malignant Biliary Obstruction. *Proc. SPIE* **2012**, 8548.

(11) Machan, L. Clinical Experience and Applications of Drug-Eluting Stents in the Noncoronary Vasculature, Bile Duct and Esophagus. *Adv. Drug Delivery Rev.* **2006**, *58*, 447−462.

(12) Huang, Y.; Venkatraman, S. S.; Boey, F. Y. C.; Lahti, E. M.; Umashankar, P. R.; Mohanty, M.; Arumugam, S.; Khanolkar, L.; Vaishnav, S. In Vitro and in Vivo Performance of a Dual Drug-Eluting Stent (DDES). *Biomaterials* **2010**, *31*, 4382−4391.

(13) Chao, Y.-K.; Liu, K.-S.; Wang, Y.-C.; Huang, Y.-L.; Liu, S.-J. Biodegradable Cisplatin-Eluting Tracheal Stent for Malignant Airway Obstruction in Vivo and in Vitro Studies. *Chest* **2013**, *144*, 193−199.

(14) Chen, M.-C.; Liu, C.-T.; Tsai, H.-W.; Lai, W.-Y.; Chang, Y.; Sung, H.-W. Mechanical Properties, Drug Eluting Characteristics and in Vivo Performance of a Genipin-Crosslinked Chitosan Polymeric Stent. *Biomaterials* **2009**, *30*, 5560−5571.

(15) Ganapathy, V.; Thangaraju, M.; Prasad, P. D. Nutrient Transporters in Cancer: Relevance to Warburg Hypothesis and Beyond. *Pharmacol. Ther.* **2009**, *121*, 29−40.

(16) Warburg, O. Origin of Cancer Cells. *Science* **1956**, *123*, 309−314.

(17) Diaz-Ruiz, R.; Rigoulet, M.; Devin, A. The Warburg and Crabtree Effects: On the Origin of Cancer Cell Energy Metabolism and of Yeast Glucose Repression. *Biochim. Biophys. Acta, Bioenerg.* **2011**, *1807*, 568−576.

(18) Harguindey, S.; Orive, G.; Pedraz, J. L.; Paradiso, A.; Reshkin, S. J. The Role of pH Dynamics and the Na^+/H^+ Antiporter in the Etiopathogenesis and Treatment of Cancer. Two Faces of the Same Coin - One Single Nature. *Biochim. Biophys. Acta, Rev. Cancer* **2005**, *1756*, 1−24.

(19) Yu, X.; Yang, X.; Horte, S.; Kizhakkedathu, J. N.; Brooks, D. E. A pH and Thermosensitive Choline Phosphate-based Delivery Platform Targeted to the Acidic Tumor Microenvironment. *Biomaterials* **2014**, *35*, 278−286.

(20) Chen, H.; MacDonald, R. C.; Li, S.; Krett, N. L.; Rosen, S. T.; O'Halloran, T. V. Lipid Encapsulation of Arsenic Trioxide Attenuates Cytotoxicity and Allows for Controlled Anticancer Drug Release. *J. Am. Chem. Soc.* **2006**, *128*, 13348−13349.

(21) Ambrogi, V.; Perioli, L.; Ricci, M.; Pulcini, L.; Nocchetti, M.; Giovagnoli, S.; Rossi, C. Eudragit (R) and Hydrotalcite-like Anionic Clay Composite System for Diclofenac Colonic Delivery. *Microporous Mesoporous Mater.* **2008**, *115*, 405−415.

(22) Fan, G.; Li, F.; Evans, D. G.; Duan, X. Catalytic Applications of Layered Double Hydroxides: Recent Advances and Perspectives. *Chem. Soc. Rev.* **2014**, *43*, 7040−7066.

(23) Li, C.; Wei, M.; Evans, D. G.; Duan, X. Layered Double Hydroxide-based Nanomaterials as Highly Efficient Catalysts and Adsorbents. *Small* **2014**, *10*, 4469−4486.

(24) Long, X.; Xiao, S.; Wang, Z.; Zheng, X.; Yang, S. Co Intake Mediated Formation of Ultrathin Nanosheets of Transition Metal LDH - An Advanced Electrocatalyst for Oxygen Evolution Reaction. *Chem. Commun. (Cambridge, U. K.)* **2015**, *51*, 1120−1123.

(25) Liu, Y.; Wang, N.; Pan, J. H.; Steinbach, F.; Caro, J. In Situ Synthesis of MOF Membranes on ZnAl-CO_3 LDH Buffer Layer-Modified Substrates. *J. Am. Chem. Soc.* **2014**, *136*, 14353−14356.

(26) Sahoo, P.; Ishihara, S.; Yamada, K.; Deguchi, K.; Ohki, S.; Tansho, M.; Shimizu, T.; Eisaku, N.; Sasai, R.; Labuta, J.; Ishikawa, D.; Hill, J. P.; Ariga, K.; Bastakoti, B. P.; Yamauchi, Y.; Iyi, N. Rapid Exchange between Atmospheric CO_2 and Carbonate Anion

DOI: 10.1021/acsami.5b01087
ACS Appl. Mater. Interfaces 2015, 7, 7843−7854

Intercalated within Magnesium rich Layered Double Hydroxide. *ACS Appl. Mater. Interfaces* **2014**, *6*, 18352−18359.
(27) Wang, Q.; O'Hare, D. Recent Advances in the Synthesis and Application of Layered Double Hydroxide (LDH) Nanosheets. *Chem. Rev. (Washington, DC, U. S.)* **2012**, *112*, 4124−4155.
(28) Zhao, M.-Q.; Zhang, Q.; Huang, J.-Q.; Wei, F. Hierarchical Nanocomposites Derived from Nanocarbons and Layered Double Hydroxides - Properties, Synthesis, and Applications. *Adv. Funct. Mater.* **2012**, *22*, 675−694.
(29) Hu, H.; Wang, X. B.; Xu, S. L.; Yang, W. T.; Xu, F. J.; Shen, J.; Mao, C. Preparation and Evaluation of Well-Defined Hemocompatible Layered Double Hydroxide-Poly(sulfobetaine) Nanohybrids. *J. Mater. Chem.* **2012**, *22*, 15362−15369.
(30) Liang, R.; Wei, M.; Evans, D. G.; Duan, X. Inorganic Nanomaterials for Bioimaging, Targeted Drug Delivery and Therapeutics. *Chem. Commun. (Cambridge, U. K.)* **2014**, *50*, 14071−14081.
(31) Zhao, Z.; Qi, Y.; Wei, M.; Zhang, F.; Xu, S. Layer-by-Layer Assembly and Morphological Characterizations of DNA/Layered Double Hydroxide Thin Films. *Mater. Lett.* **2012**, *78*, 62−65.
(32) Lin, J.-K.; Uan, J.-Y.; Wu, C.-P.; Huang, H.-H. Direct Growth of Oriented Mg-Fe Layered Double Hydroxide (LDH) on Pure Mg Substrates and in Vitro Corrosion and Cell Adhesion Testing of LDH-Coated Mg Samples. *J. Mater. Chem.* **2011**, *21*, 5011−5020.
(33) Yao, F.; Hu, H.; Xu, S.; Huo, R.; Zhao, Z.; Zhang, F.; Xu, F. Preparation and Regulating Cell Adhesion of Anion-Exchangeable Layered Double Hydroxide Micropatterned Arrays. *ACS Appl. Mater. Interfaces* **2015**, *7*, 3882−3887.
(34) Park, D.-H.; Kim, J.-E.; Oh, J.-M.; Shul, Y.-G.; Choy, J.-H. DNA Core@Inorganic Shell. *J. Am. Chem. Soc.* **2010**, *132*, 16735−16736.
(35) Shao, M.; Ning, F.; Zhao, J.; Wei, M.; Evans, D. G.; Duan, X. Preparation of Fe_3O_4@SiO_2@Layered Double Hydroxide Core-Shell Microspheres for Magnetic Separation of Proteins. *J. Am. Chem. Soc.* **2012**, *134*, 1071−1077.
(36) Munoz, A.; Costa, M. Elucidating the Mechanisms of Nickel Compound Uptake: A Review of Particulate and Nano-Nickel Endocytosis and Toxicity. *Toxicol. Appl. Pharmacol.* **2012**, *260*, 1−16.
(37) Davidson, T.; Chen, H. B.; Garrick, M. D.; D'Angelo, G.; Costa, M. Soluble Nickel Interferes with Cellular Iron Homeostasis. *Mol. Cell. Biochem.* **2005**, *279*, 157−162.
(38) Zhang, W. H.; Guo, X. D.; He, J.; Qian, Z. Y. Preparation of Ni(II)/Ti(IV) Layered Double Hydroxide at High Supersaturation. *J. Eur. Ceram. Soc.* **2008**, *28*, 1623−1629.
(39) Li, B.; Zhao, Y.; Zhang, S.; Gao, W.; Wei, M. Visible-Light-Responsive Photocatalysts toward Water Oxidation Based on NiTi-Layered Double Hydroxide/Reduced Graphene Oxide Composite Materials. *ACS Appl. Mater. Interfaces* **2013**, *5*, 10233−10239.
(40) Gu, Y.; Lu, Z.; Chang, Z.; Liu, J.; Lei, X.; Li, Y.; Sun, X. NiTi Layered Double Hydroxide Thin Films for Advanced Pseudocapacitor Electrodes. *J. Mater. Chem. A* **2013**, *1*, 10655−10661.
(41) Liang, Z. H.; Zhu, Y. J.; Hu, X. L. β-Nickel Hydroxide Nanosheets and Their Thermal Decomposition to Nickel Oxide Nanosheets. *J. Phys. Chem. B* **2004**, *108*, 3488−3491.
(42) AN, M. Characterization of β-$Ni(OH)_2$ by XPS. *Surf. Sci. Spectra* **1994**, *3*, 8.
(43) An, Y.; Li, Z.; Wang, D.; Shen, J. Origin of the Visible Light Absorption of Co^{2+} and NH_4^+ Co-Doped Hydrogen Titanate Nanotube Thin Films. *Phys. Status Solidi B* **2013**, *250*, 1592−1598.
(44) Lo, P. H.; Tsai, W. T.; Lee, J. T.; Hung, M. P. The Electrochemical-Behavior of Electroless-Plated Ni-P Alloys in Concentrated NaOH Solution. *J. Electrochem. Soc.* **1995**, *142*, 91−96.
(45) Camposeco, R.; Castillo, S.; Mejia, I.; Mugica, V.; Carrera, R.; Montoya, A.; Moran-Pineda, M.; Navarrete, J.; Gomez, R. Active TiO_2 Nanotubes for Co Oxidation at Low Temperature. *Catal. Commun.* **2012**, *17*, 81−88.
(46) Nolan, M.; Tofail, S. A. M. Density Functional Theory Simulation of Titanium Migration and Reaction with Oxygen in the Early Stages of Oxidation of Equiatomic NiTi Alloy. *Biomaterials* **2010**, *31*, 3439−3448.
(47) Huan, Z.; Fratila-Apachitei, L. E.; Apachitei, I.; Duszczyk, J. Effect of Aging Treatment on the in Vitro Nickel Release from Porous Oxide Layers on NiTi. *Appl. Surf. Sci.* **2013**, *274*, 266−272.
(48) Rao, X.; Chu, C. L.; Chung, C. Y.; Chu, P. K. Hydrothermal Growth Mechanism of Controllable Hydrophilic Titanate Nanostructures on Medical NiTi Shape Memory Alloy. *J. Mater. Eng. Perform.* **2012**, *21*, 2600−2606.
(49) Kang, J. H.; Zhang, D. W.; Chen, J.; Liu, Q.; Lin, C. J. Antioxidants and Trichostatin a Synergistically Protect against in Vitro Cytotoxicity of Ni^{2+} in Human Hepatoma Cells. *Toxicol. In Vitro* **2005**, *19*, 173−182.
(50) Riley, M. R.; Boesewetter, D. E.; Kim, A. M.; Sirvent, F. P. Effects of Metals Cu, Fe, Ni, V, and Zn on Rat Lung Epithelial Cells. *Toxicology* **2003**, *190*, 171−184.
(51) Safavi, A.; Maleki, N.; Farjami, E. Fabrication of a Glucose Sensor Based on a Novel Nanocomposite Electrode. *Biosens. Bioelectron.* **2009**, *24*, 1655−1660.
(52) Zhao, C.; Shao, C.; Li, M.; Hao, K. Flow-Injection Analysis of Glucose without Enzyme Based on Electrocatalytic Oxidation of Glucose at a Nickel Electrode. *Talanta* **2007**, *71*, 1769−1773.
(53) Ispas, C.; Andreescu, D.; Patel, A.; Goia, D. V.; Andreescu, S.; Wallace, K. N. Toxicity and Developmental Defects of Different Sizes and Shape Nickel Nanoparticles in Zebrafish. *Environ. Sci. Technol.* **2009**, *43*, 6349−6356.
(54) Forti, E.; Salovaara, S.; Cetin, Y.; Bulgheroni, A.; Tessadri, R.; Jennings, P.; Pfaller, W.; Prieto, P. In Vitro Evaluation of the Toxicity Induced by Nickel Soluble and Particulate Forms in Human Airway Epithelial Cells. *Toxicol. In Vitro* **2011**, *25*, 454−461.
(55) McFate, T.; Mohyeldin, A.; Lu, H.; Thakar, J.; Henriques, J.; Halim, N. D.; Wu, H.; Schell, M. J.; Tsang, T. M.; Teahan, O.; Zhou, S.; Califano, J. A.; Jeoung, N. H.; Harris, R. A.; Verma, A. Pyruvate Dehydrogenase Complex Activity Controls Metabolic and Malignant Phenotype in Cancer Cells. *J. Biol. Chem.* **2008**, *283*, 22700−22708.
(56) Di Sario, A.; Bendia, E.; Omenetti, A.; De Minicis, S.; Marzioni, M.; Kleemann, H. W.; Candelaresi, C.; Saccomanno, S.; Alpini, G.; Benedetti, A. Selective Inhibition of Ion Transport Mechanisms Regulating Intracellular pH Reduces Proliferation and Induces Apoptosis in Cholangiocarcinoma Cells. *Dig. Liver Dis.* **2007**, *39*, 60−69.
(57) Fukumura, D.; Jain, R. K. Tumor Microvasculature and Microenvironment: Targets for Anti-angiogenesis and Normalization. *Microvasc. Res.* **2007**, *74*, 72−84.
(58) Tallkvist, J.; Bowlus, C. L.; Lonnerdal, B. Effect of Iron Treatment on Nickel Absorption and Gene Expression of the Divalent Metal Transporter (DMT1) by Human Intestinal Caco-2 Cells. *Pharmacol. Toxicol. (Oxford, U. K.)* **2003**, *92*, 121−124.
(59) Garrick, M. D.; Dolan, K. G.; Horbinski, C.; Ghio, A. J.; Higgins, D.; Porubcin, M.; Moore, E. G.; Hainsworth, L. N.; Umbreit, J. N.; Conrad, M. E.; Feng, L.; Lis, A.; Roth, J. A.; Singleton, S.; Garrick, L. M. DMT1: A Mammalian Transporter for Multiple Metals. *Biometals* **2003**, *16*, 41−54.
(60) Mackenzie, B.; Takanaga, H.; Hubert, N.; Rolfs, A.; Hediger, M. A. Functional Properties of Multiple Isoforms of Human Divalent Metal-Ion Transporter 1 (DMT1). *Biochem. J.* **2007**, *403*, 59−69.
(61) Illing, A. C.; Shawki, A.; Cunningham, C. L.; Mackenzie, B. Substrate Profile and Metal-Ion Selectivity of Human Divalent Metal-Ion Transporter-1. *J. Biol. Chem.* **2012**, *287*, 30485−30496.
(62) Wang, W.; Zhao, L.; Ma, Q.; Wang, Q.; Chu, P. K.; Zhang, Y. The Role of the Wnt/β-Catenin Pathway in the Effect of Implant Topography on MG63 Differentiation. *Biomaterials* **2012**, *33*, 7993−8002.
(63) Wang, W.; Zhao, L.; Wu, K.; Ma, Q.; Mei, S.; Chu, P. K.; Wang, Q.; Zhang, Y. The Role of Integrin-Linked Kinase/β-Catenin Pathway in the Enhanced MG63 Differentiation by Micro/Nano-textured Topography. *Biomaterials* **2013**, *34*, 631−640.
(64) Viswanathan, P.; Chirasatitsin, S.; Ngamkham, K.; Engler, A. J.; Battaglia, G. Cell Instructive Microporous Scaffolds through Interface Engineering. *J. Am. Chem. Soc.* **2012**, *134*, 20103−20109.

DOI: 10.1021/acsami.5b01087
ACS Appl. Mater. Interfaces 2015, 7, 7843−7854

(65) Biggs, M. J. P.; Richards, R. G.; Dalby, M. J. Nanotopographical Modification: A Regulator of Cellular Function through Focal Adhesions. *Nanomedicine (N. Y., NY, U. S.)* **2010**, *6*, 619−633.
(66) Arnold, M.; Cavalcanti-Adam, E. A.; Glass, R.; Blummel, J.; Eck, W.; Kantlehner, M.; Kessler, H.; Spatz, J. P. Activation of Integrin Function by Nanopatterned Adhesive Interfaces. *ChemPhysChem* **2004**, *5*, 383−388.
(67) Lee, J.; Kang, B. S.; Hicks, B.; Chancellor, T. F., Jr.; Chu, B. H.; Wang, H.-T.; Keselowsky, B. G.; Ren, F.; Lele, T. P. The Control of Cell Adhesion and Viability by Zinc Oxide Nanorods. *Biomaterials* **2008**, *29*, 3743−3749.

DOI: 10.1021/acsami.5b01087
ACS Appl. Mater. Interfaces 2015, 7, 7843−7854